

Article

The Influence of CO₂ Physical Properties on Casing and Its Prediction Method

Meng Cai ^{1,*}, Junliang Li ¹, Wenhai Ma ¹, Nan Zhang ¹, Peng Wang ¹, Xiaochuan Zhang ¹, Shangyu Yang ² and Jing Cao ^{2,*}

¹ Daqing Oil Field Production Technology Institute, Daqing 163000, China

² State Key Laboratory of Oil and Gas Equipment, CNPC Tubular Goods Research Institute, Xi'an 710077, China

* Correspondence: cycaimeng@petrochina.com.cn (M.C.); caojing412@126.com (J.C.);

Tel.: +86-29-81887953 (J.C.)

Abstract: In order to reveal the physical properties of CO₂ under actual formation conditions, this paper establishes a mathematical model of the temperature field and pressure field in the wellbore under CO₂ injection conditions, optimizes the state equation of CO₂ physical-property parameters, calculates the change trend of CO₂ density, viscosity, and compression factor along the wellbore, and obtains the influence law of CO₂ corrosion on the casing and interface. The viscosity showed a downward trend along the well depth; the compression factor showed an upward trend. The surfaces of the three casings were smooth and flat without obvious defects, the cement structure was dense, and there was no obvious pore structure. After corrosion, with the increase of Cr content, the change of interfacial corrosion decreases. The morphology of the Q125 and 3Cr interface is loose after corrosion, while there is no obvious change in the 13Cr interface. With the prolongation of corrosion time, low wellbore internal pressure easily causes casing yield, and high wellbore internal pressure easily causes cement-sheath compression failure. The circumferential stress of the casing increases with the corrosion time extension, and the radial stress of the casing and cement sheath decreases first and then increases with the corrosion time. The compressive strength of the cement sheath does not exceed the compressive strength.

Keywords: pressure field; casing damage; corrode; stress



Citation: Cai, M.; Li, J.; Ma, W.; Zhang, N.; Wang, P.; Zhang, X.; Yang, S.; Cao, J. The Influence of CO₂ Physical Properties on Casing and Its Prediction Method. *Processes* **2024**, *12*, 768. <https://doi.org/10.3390/pr12040768>

Academic Editor: Carlos Sierra Fernández

Received: 29 February 2024

Revised: 29 March 2024

Accepted: 6 April 2024

Published: 11 April 2024



Copyright: © 2024 by the authors. Licensee MDPI, Basel, Switzerland. This article is an open access article distributed under the terms and conditions of the Creative Commons Attribution (CC BY) license (<https://creativecommons.org/licenses/by/4.0/>).

1. Introduction

During the development of some oil wells in the Gulong shale oil field, CO₂ injection composite fracturing was adopted, which can achieve the dual effect of ensuring the national energy supply and reducing carbon emissions. It will have a certain demonstration role in achieving the “carbon neutrality” goal. However, during the CO₂ injection process, the corrosion of the wellbore caused by CO₂ could not be ignored.

Many domestic and foreign researchers have conducted research on CO₂ corrosion. Zhang et al. [1] analyzed the effects of temperature drop and salt creep on wellbore integrity during CO₂ sequestration. The stress-equivalent method was used to equate the actual stress of the wellbore cement sheath with the simulated borehole cement. Amour et al. [2] indicated that the accurate characterization of the porosity distribution in the reservoir and the potential mechanical weakening of chalk by CO₂ were essential for reliable wellbore integrity analyses. Lüftenegger et al. [3] studied the effects of CO₂ injection into a depleted gas field. Gu et al. [4] illustrated that the integrity of the cement sheath is critical to the safety and efficiency of CO₂ capture and storage technologies. The failure of a cement-casing microannulus is considered to be one of the most important mechanisms affecting the integrity of the wellbore and can lead to the leakage of carbon dioxide and other fluids. Zhang et al. [5] indicated that, during long-term CO₂ injection, the sealing effect of the cement would decrease gradually, and the cement sheath was more likely to fail under external loads arising from wellbore pressure and temperature variations. Wang et al. [6]

found the long-term integrity of the cemented surface of the cement plug was directly related to the risk of CO₂ leakage. These studies focus on the damage to wellbore integrity caused by changes in wellbore pressure and temperature under CO₂ injection.

Meng et al. [7] showed that compared with water, liquid CO₂ more easily initiated the microannulus. Xie et al. [8] found that a challenge in the CO₂ storage reservoir was how to identify and prevent leakage. With a constant in situ stress and different annulus pressures (before cementing), the cemented annulus behaved in a different manner. Wise et al. [9] showed that the setting stress and the pore pressure in the cement that developed during hydration caused the most potential for debonding. Wan et al. [10] compared CO₂ storage by fracturing different fracture networks. In the case of CO₂ injection for enhanced oil recovery, this process has less impact on CO₂ storage. Sobolik et al. [11] established geomechanical modeling to predict wellbore stresses and strains for the design of wellbore seal repair materials for use at a CO₂ injection site. During the injection of carbon dioxide, changes in temperature may lead to stress changes that can further damage the well, threatening its integrity [12–14]. This research has shown that CO₂ injection into the wellbore could lead to changes in wellbore stress and strain.

Models based on the coupling of geochemical and geomechanical changes were developed in order to predict the consequences of the possible losses. The model simulated the change of a rock–cement casing combination in the abandoned well of the carbon storage bank [15–17]. The possible geomechanical risks in the CCS process were outlined [18–20]. Gao et al. [21] provided theoretical guidance and analysis methods for evaluating the integrity of wellbore cement and optimizing injection parameters under CO₂ and injection conditions and described the research status of the integrity of a cement sheath with defects. Feng et al. [22] established a temperature-induced stress-induced failure model for the sealing failure of the lower cement ring. With the increase of CO₂ injection pressure, injection displacement, injection time, and injection temperature, the cement sheath is more likely to form micro-gaps, and the length of micro-gaps in the longitudinal direction also increases. Therefore, establishing a reasonable temperature and stress-induced failure model can predict the failure of cement-sheath integrity.

In this paper, the physical properties of CO₂ under different stratigraphic conditions were analyzed, the state equation of CO₂ was optimized, and the physical properties of CO₂ under different stratigraphic conditions were analyzed. The experimental analysis of the corrosion effect of CO₂ on the casing, cement stone, and interface under non-bearing conditions was carried out, the law of CO₂ corrosion rate on casing under non-bearing conditions was obtained, and the physical-property characteristics of cement and stone with different corrosion degrees were studied. The CO₂ corrosion wellbore damage prediction method was obtained, and the influence of CO₂ corrosion on the properties of cement and stone was revealed. Finally, the corrosion rate prediction model of casing and cement stone under different CO₂ concentrations, temperatures, and pressure conditions was established. It is of great significance to study the influence of CO₂ on wellbore integrity and the prediction method.

2. The Effect of CO₂ on Wellbore Integrity Failure

In June 2021, the predicted geological reserves of 1.268 billion tons of Gulong shale oil passed the review of PetroChina, realizing the first step in the transformation of resources into reserves. In the development process of some oil wells of Gulong shale oil, the method of adding CO₂ composite fracturing can be used to ensure the national energy supply and reduce carbon emissions, and it will play a certain exemplary role in the realization of the goal of “carbon neutrality”. Affected by CO₂, the failure of wellbore integrity is manifested in three situations: downhole casing is prone to uniform corrosion, pitting, perforation, and even corrosion fracture in the CO₂ environment. The injected CO₂ is dissolved in the formation water to form carbonic acid corroded cement stone, which causes the degradation of the mechanical properties of the cement sheath and makes the cementing cement sheath lose its sealing effect. After CO₂ corrosion, the wall thickness of

the casing is reduced, the mechanical properties of the cement and stone are reduced, and the pressure-bearing capacity of the wellbore is weakened during the fracturing process and under the conditions of long-term CO₂ corrosion, Figure 1a shows the failure photos of downhole casing in CO₂ environment. In view of the above situation, it is necessary to clarify the phase characteristic distribution law of CO₂ along the temperature and pressure condition of the wellbore, the corrosion law of the string and cementing cement stone in the downhole CO₂ environment (Figure 1b), and the prediction of the wellbore pressure bearing capacity under the condition of CO₂ fracturing and long-term CO₂ corrosion, and to put forward corresponding adjustment measures.

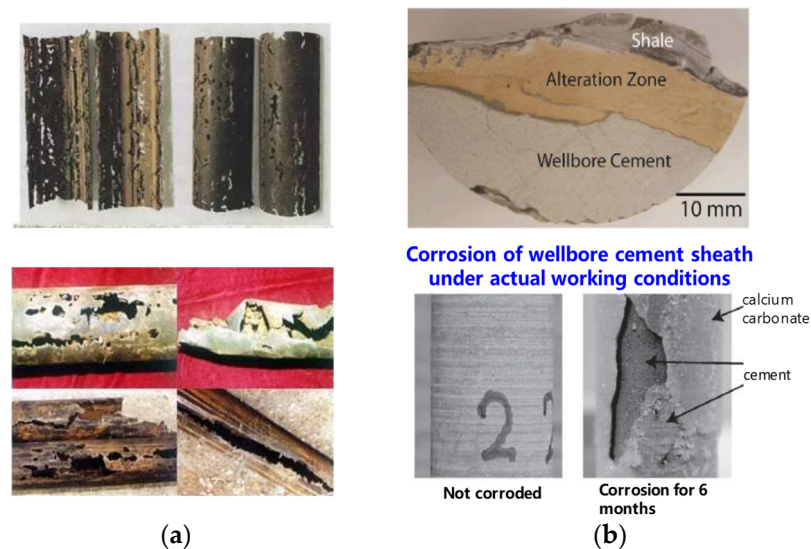


Figure 1. Failure photos of downhole casing in CO₂ environment. (a) casing corrosion (b) cement stone corrosion.

3. Physical Properties of CO₂ under Actual Stratigraphic Conditions

3.1. Physical Properties of CO₂ under Actual Stratigraphic Conditions

Due to the gas–liquid duality of supercritical CO₂, RK, SRK, PR and Span-Wagner calculation equations can accurately calculate the density of supercritical CO₂ within a certain range. Therefore, four methods are screened. Based on the literature data, the density values under different temperatures and pressures are calculated using the three density calculation formulas initially selected after research and compared with the values in the NIST database, as shown in Figure 2a. The average relative error is used as the measurement standard for accuracy, and the CO₂ density calculation model with the highest accuracy is selected. The average relative error between the calculated results of the SW model and the measured values is the smallest, as shown in Figure 2b, so Equation (1) is used to calculate CO₂ density in subsequent calculations. The SW equation has a wide range of applications, but the density is implicit, and the calculation is more complicated.

The CO₂ density—SW equation is:

$$\frac{M \cdot p(\delta, \tau)}{\rho RT} = 1 + \delta \phi_{\delta}^r \quad (1)$$

where M is the molar mass, p is pressure, R is gas constant, T is temperature, and Φ_{δ} is Helmholtz free energy.

The CO₂ viscosity at different temperatures and pressures can be calculated using the LBC model, Lee model, and Dempsey model, respectively [23]. The average relative error between the calculated results of the Lee model and the measured values is the smallest, as shown in Figure 3, so Equation (2) is used to calculate CO₂ viscosity in subsequent calculations. The Lee model can describe the effects of temperature and pressure on viscosity at

the same time, but it does not take into account the interaction between molecules, and the deviation is large at low temperatures.

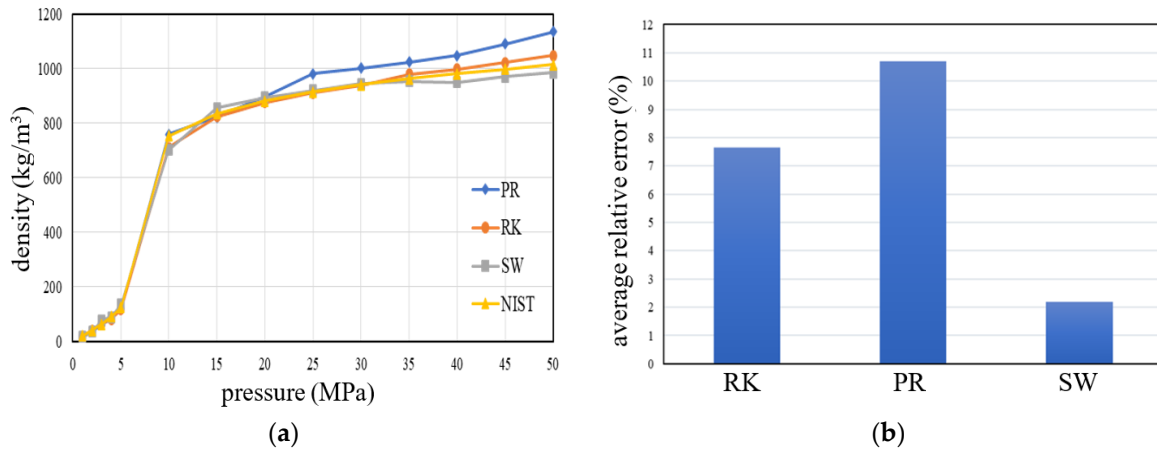


Figure 2. Density calculation results under different models. (a) Calculation results of various models at 30 °C. (b) Average relative error of each model.

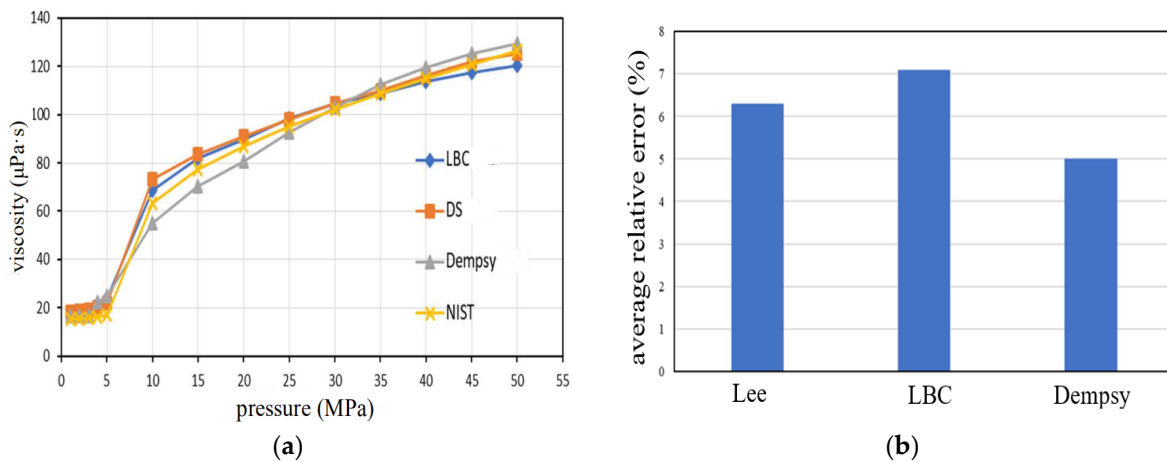


Figure 3. Viscosity calculation results under different models. (a) Calculation results of various models at 30 °C. (b) Average relative error of each model.

The CO₂ Viscosity—Lee Model is:

$$\mu_g = 10^{-4} K \exp(X \rho_g^Y) \quad (2)$$

where μ_g is the viscosity of the gas, $\mu\text{Pa}\cdot\text{s}$; ρ_g is CO₂ density under standard conditions, g/cm^3 , X , Y , and K are the associated parameters.

The compression factor, also known as the compression coefficient or deviation coefficient, refers to the ratio of gas volume to ideal gas studied under the same temperature, pressure, and mole number conditions. The CO₂ compression factor under different temperatures and pressures is calculated using the PR model, RK model, and SW model respectively [24]. The RK model has the smallest average relative error between the calculated results and the measured values, as shown in Figure 4. Therefore, Equation (3) is used to calculate the CO₂ compression factor in subsequent calculations. The RK model data is easy to obtain, easy to program and calculate, saving calculation time and cost.

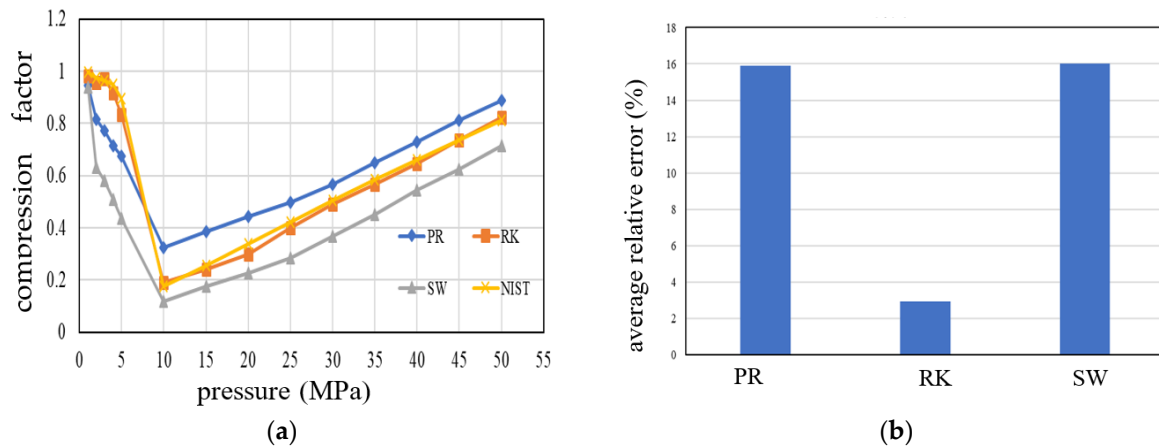


Figure 4. Compression-factor calculation results under different models. (a) Calculation results of various models at 30 °C. (b) Average relative error of each model.

The CO₂ compression factor RK model is:

$$\alpha = \frac{1}{\sqrt{T_{scf}}} \quad (3)$$

where T_{scf} is the standard temperature, K.

3.2. Mathematical Model of Wellbore Temperature Field and Pressure Field

3.2.1. Wellbore Heat-Transfer Model

The heat transfer inside the wellbore is a one-dimensional steady-state heat transfer. Unit heat loss from the center of the tubing to any position in the wellbore:

$$dQ = \frac{\nabla T}{R} dz \quad (4)$$

The total thermal resistance from the center of the tubing to the outer wall of the cement ring is:

$$R = \frac{1}{2\pi r_1} \left[\frac{r_1}{h_{gas} r_0} + \frac{r_1}{\lambda_{tub}} \ln \frac{r_1}{r_0} + \frac{r_1}{r_2 (h_c + h_r)} + \frac{r_1}{\lambda_{cas}} \ln \frac{r_3}{r_2} + \frac{r_1}{\lambda_{cem}} \ln \frac{r_4}{r_3} \right] \quad (5)$$

In the formula, $\frac{r_1}{h_{gas} r_0}$ is the produced gas part, $\frac{r_1}{\lambda_{tub}} \ln \frac{r_1}{r_0}$ is the tubing part, $\frac{r_1}{r_2 (h_c + h_r)}$ is the annular part, $\frac{r_1}{\lambda_{cas}} \ln \frac{r_3}{r_2}$ is the cement-sheath part, and $\frac{r_1}{\lambda_{cem}} \ln \frac{r_4}{r_3}$ is the formation part. The heat transfer inside the formation is one-dimensional unsteady heat transfer:

$$dQ = \frac{2\pi\lambda_f (T_2 - T_f)}{f(t)} dz \quad (6)$$

Tubing inner wall temperature:

$$T_4 = \frac{\lambda_f T_f + T_{gas} r_1 U f(t)}{r_2 U f(t) + \lambda_f} \quad (7)$$

3.2.2. Tubing Inner Wall Temperature

Unsteady pressure drop model of CO₂ injection into the wellbore:

The equation for the conservation of mass is:

$$\frac{\partial \rho_1}{\partial t} + \frac{1}{r_1} \frac{\partial (r_1 \rho_1 v_2)}{\partial r_1} + \frac{\partial (\rho_1 v_1)}{\partial z} = 0 \quad (8)$$

where v_1 is the radial velocity, and v_2 is the axial velocity.

The equation for the Conservation of Momentum is:

$$\frac{\partial}{\partial t}(\rho_1 w) + \frac{1}{r_1} \frac{\partial}{\partial r_1}(r_1 \rho_1 u w) + \frac{\partial}{\partial z}(\rho_1 w w) = -\frac{\partial p_1}{\partial z} + \frac{1}{r_1} \frac{\partial}{\partial r_1}\left(r_1 \mu \frac{\partial w}{\partial r_1}\right) + \frac{\partial}{\partial z}\left(\mu \frac{\partial w}{\partial z}\right) \quad (9)$$

Unsteady Voltage Drop Model:

$$\frac{dp_1}{dz} = \rho_1 g \sin \theta - f \frac{\rho_1 w^2}{4r_1} - \rho_1 v_1 \frac{\partial w_1}{\partial t} \quad (10)$$

Friction coefficient:

$$\frac{1}{\sqrt{f}} = -2 \lg \left[\frac{\Delta}{3.7065d} - \frac{5.0452}{\text{Re}} \lg \left(\frac{1}{2.8257} \left(\frac{\Delta}{d} \right)^{1.1098} + \frac{5.8506}{\text{Re}^{0.8981}} \right) \right] \quad (11)$$

where f is friction coefficient, d is inner diameter of casing, m; and Re is fluid Reynolds number.

4. The Influence of CO₂ Corrosion on Casing, Cement and Stone, and Interface

4.1. The Influence of CO₂ Partial Pressure and Cl⁻ Concentration on CO₂ Corrosion Casing

With the increase of the partial pressure of CO₂, the amount of CO₂ dissolved in water increases, and the pH of the aqueous solution decreases, thereby increasing the corrosivity of the solution, and the corrosion rate increases with the increase of the partial pressure of v . Based on the existing literature, it is concluded that the corrosion rate of the casing varies with the Cl⁻ concentration. As shown in Figure 5, the Cl⁻ radius is small and the penetration is strong, which can penetrate the corrosion-product film and penetrate into the surface of the metal matrix, promoting the dissolution of Fe²⁺ under the film to produce H⁺, thereby promoting the electrochemical corrosion of the metal matrix, and easily form soluble chloride with the cations in the passivation film to destroy the corrosion-protection film.

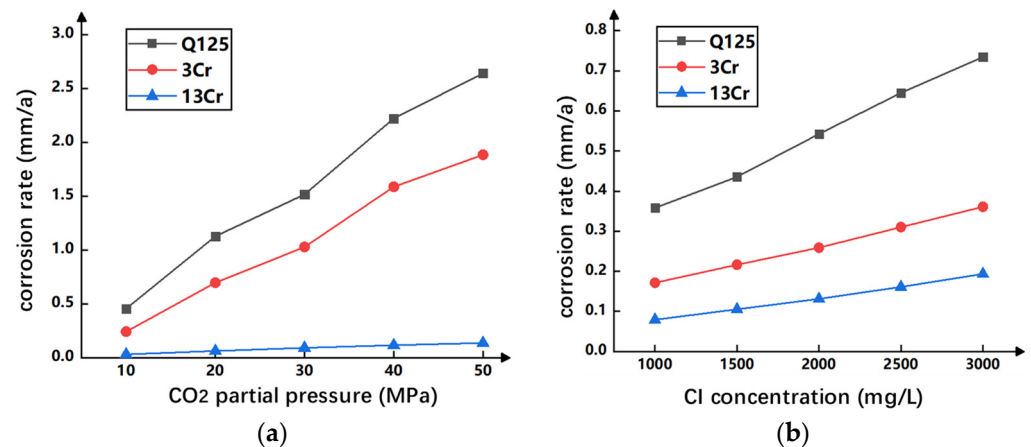


Figure 5. Casing corrosion rate, CO₂ partial pressure change, and Cl⁻ concentration curve. (a) The corrosion rate of the casing varies. (b) The corrosion rate of the casing with the partial pressure of CO₂ varies with the Cl⁻ concentration.

4.2. Mechanism and Laws of CO₂ Corrosion of Cement Stone

The corrosion mechanism of CO₂ on cement can be divided into the kinetic reaction mechanism and mass transfer mechanism. With the transfer of acidic substances and the progress of the corrosion reaction, the entire corrosion process exhibits several effects. Among them, the kinetic reaction mechanism mainly manifests as carbonization, the mass transfer mechanism manifests as leaching and decalcification, and the neutralization

mechanism both have two mechanisms. The combination of several specific actions results in the overall corrosion effect.

1. Carbonization effect

After the oil-well cement stone comes into contact with corrosive fluids that dissolve CO_2 , Ca^{2+} in the cement pore fluid reacts with hydrogen ions and bicarbonate ions to form calcium carbonate first. With the carbonization of different components, different forms of calcium carbonate are formed. Calcium hydroxide undergoes a carbonization reaction to form calcite, and some hydrated calcium silicate reacts to form aragonite and vaterite. The formed calcium carbonate fills the pores of the cement stone, reduces the porosity of the cement stone, improves the strength of the early corroded cement stone, and expands the internal space of the cement stone, forming the cracks;

2. Neutralization effect

After the formation fluid comes into contact with the cement matrix, CO_2 dissolves to form a carbonate solution, which reduces the initial pH value of the cement–fluid interface. The initial pH value of the pore fluid in the cement matrix is 12~13. As hydrogen ions in the acidic corrosive fluid migrate into the cement, the pH value of the fluid in the cement pores decreases. The cement hydration products that were originally stable in an alkaline environment gradually lose stability and react to CaCO_3 . As the dissolved Ca^{2+} and OH^- in the solution are consumed, the C-H dissolves and releases Ca^{2+} and OH^- , buffering the acidity of the water. The Ca/Si ratio of the C-S-H component gradually decreases, and the reaction reaches the final stage with the remaining amorphous SiO_2 . When the neutralization reaches a certain degree, the calcium carbonate generated by carbonization will react and decompose under high concentrations of hydrogen ions to form $\text{Ca}(\text{HCO}_3)_2$.

As the corrosion time increases, the generation rate of CaCO_3 gradually decreases. The interface between the amorphous SiO_2 enrichment zone and the CaCO_3 deposition layer, the interface between the CaCO_3 deposition layer and the $\text{Ca}(\text{OH})_2$ depletion zone, and the interface between the $\text{Ca}(\text{OH})_2$ depletion zone and the unreacted zone gradually extend towards the interior of the cement paste, but the expansion rate gradually decreases. Specifically, the corrosion rate gradually decreases. The thickness of the amorphous SiO_2 enrichment zone gradually increases, and further research is needed to determine the thickness variation patterns of the CaCO_3 deposition zone and the $\text{Ca}(\text{OH})_2$ depletion zone. In this case, the compressive strength and hardness of the cement stone are low, and many secondary microcracks will be generated inside, further increasing the overall permeability of the cement stone, resulting in a decrease in the sealing ability of the cement stone body and its bonding surface in the annulus.

4.3. Mechanism and Law of CO_2 Corrosion at Casing–Cement Stone Interface

According to Figure 6, in a short period of time, the casing indicates the formation of a film like FeCO_3 to inhibit corrosion, and with the increase of time, Ca^{2+} migrates to the surface of the casing, forming porous and loose CaCO_3 . The corrosion product CaCO_3 is continuously dissolved, and with the increase of time, Fe^{2+} migrates to the cement matrix and forms coarse-grained FeCO_3 , which affects the self-healing of cement stone. And, Fe^{2+} inhibits the formation of CaCO_3 calcite and converts it into polycrystalline aragonite or crystal stone. The corrosion products $\text{Fe}_x\text{Ca}_{1-x}\text{CO}_3$ and Fe_3O_4 are formed under high CO_2 partial pressure, which is not conducive to the corrosion resistance and integrity of the cement–casing interface.

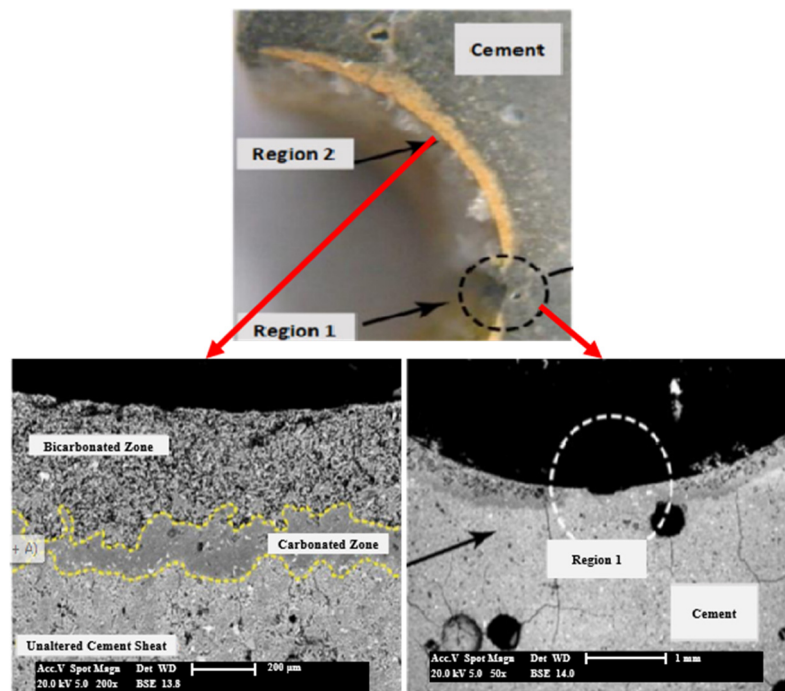
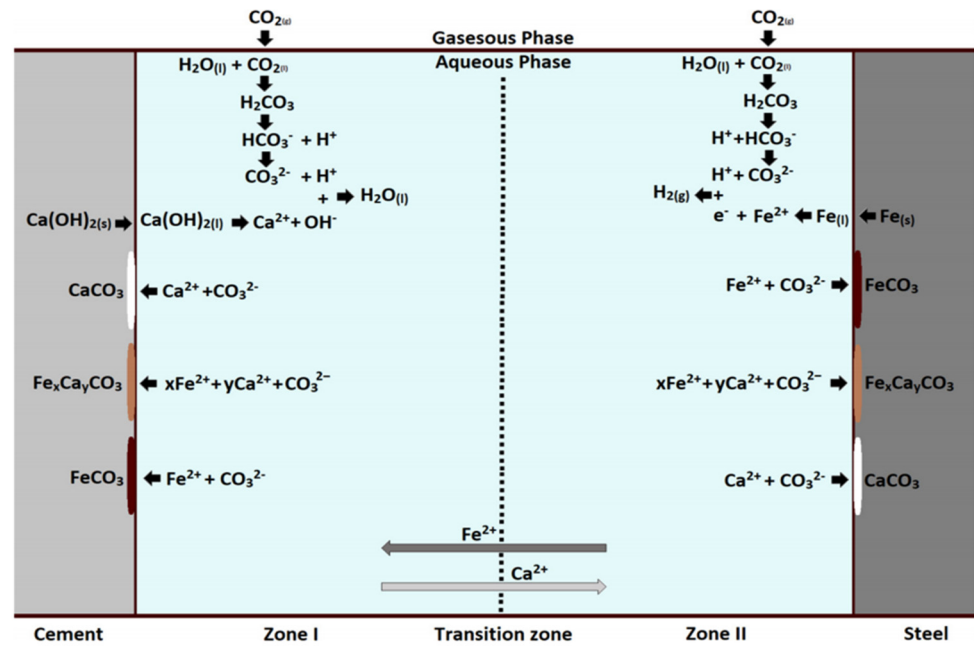


Figure 6. Interfacial corrosion mechanism and corrosion electron microscopy diagram. (a) Interfacial corrosion diagram. (b) Interfacial corrosion and uncorroded electron microscopy diagrams.

4.4. Test of Casing, Cement Stone, and Interface Properties before and after Corrosion under Non-Bearing Conditions

The experimental methodology is:

By combining the research on the reaction mechanism of CO₂ corrosion casing and cement stone, the corrosion experiments of simulated on-site temperature, pressure, and formation water salinity were carried out on the cement slurries, namely the conventional system provided on site, and the analysis of the CO₂ corrosion law of casing, cement stone, and interface was carried out according to the phase composition and microscopic

morphology of casing, cement stone, and interface before and after corrosion. Before the experiment, an electronic balance was used to record the mass of the steel sheet before corrosion. Then, different steels (3Cr, 13Cr, Q125) are placed into the reactor, and the prepared formation water is added to 2/3 of the reactor height. A pressure gauge is connected to the reactor, and the pressure value inside the reactor is recorded at this time. After the temperature is heated to the corrosion temperature (80/90/110/120 °C), open the gas boosting system, connecting valves, gas-tank valves, etc., and introduce CO₂ for 5 min to remove the air inside the reactor. The outlet valve is closed, and CO₂ is continued to the corrosion pressure (30 MPa). After the experiment, the surface of the sample is rinsed with distilled water to remove corrosive media. After removing the corrosion-product film, weigh and calculate the mass loss and average corrosion rate of the sample using an electronic balance with an accuracy of 0.1 mg. The surface-corrosion morphology is observed using scanning electron microscopy.

The experimental materials are:

The conventional system is Dalian G-grade cement + 25% quartz sand + 1.5% expansion agent + 4% toughening agent + 1.2% water loss reducing agent + 0.3% defoamer + 1.0% antifoam agent + 0.4% dispersant + 0.2% retarder.

4.4.1. Test Results of Casing Properties before and after Corrosion

As shown in Figure 7, the test results of the properties of casing before and after corrosion show that, before corrosion, the surfaces are smooth and flat without obvious defects. After corrosion, the surface of the Q125 and 3Cr casings has obvious defects and a rough and loose structure, and the morphology of the 13Cr steel is not obvious.

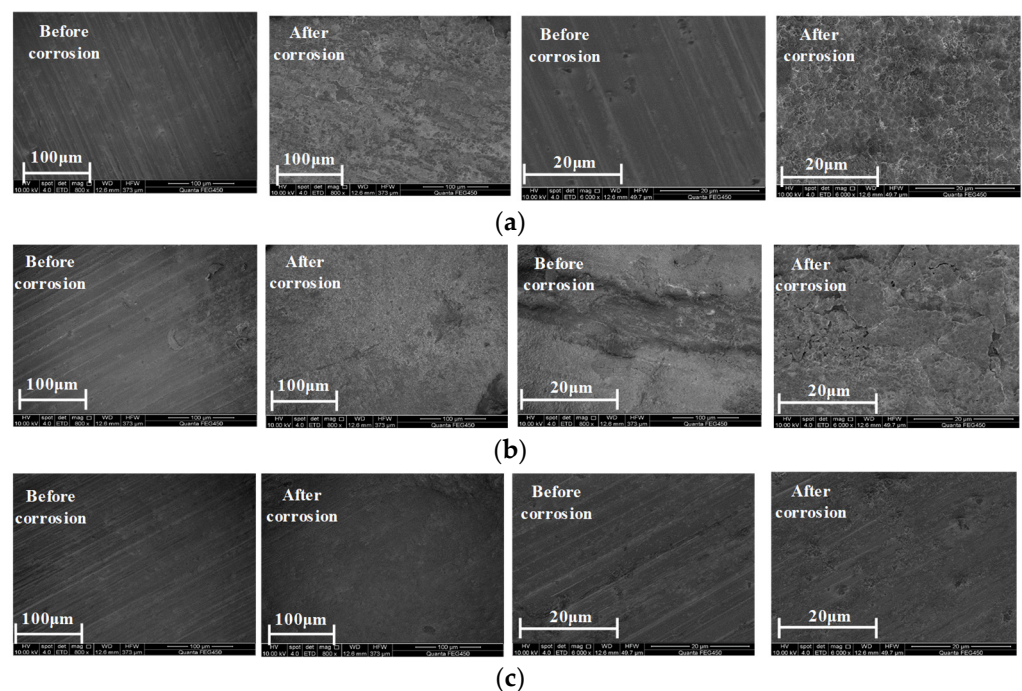


Figure 7. Surface morphology of three materials before and after corrosion. (a) Q125. (b) 3Cr. (c) 13Cr.

4.4.2. Test Results of Casing–Cement Stone Interface Properties before and after Corrosion

After corrosion, SEM electron microscopy images of the interface between Q125 and cement stone ($\times 50 \mu\text{m}$) are shown in Figure 8. The microstructure of the casing at the interface does not show significant changes, the cement structure near the interface becomes loose, and there is pore morphology at the cement interface. The bonding area shows obvious curved corrosion traces. After corrosion, SEM electron microscopy images show that the interface between the 3Cr and the cement stone does not show significant changes. Compared to Q125, the corrosion at the interface with cement stone is lighter. The

microstructure of the casing at the interface of the 13Cr and the cement shows almost no change, and compared to the corrosion at the interface between the 3Cr and the cement stone, the corrosion is more lighter. No obvious looseness is observed in the cement-stone structure near the interface, and no corrosion morphology such as pores appears at the cement-stone interface.

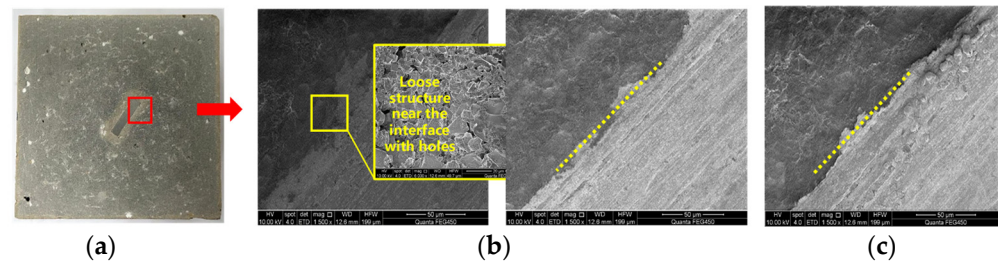


Figure 8. SEM images of the surfaces of three materials before and after corrosion. (a) Q125. (b) 3Cr. (c) 13Cr.

4.4.3. Effect of CO₂ on Casing Corrosion Rate Test under Non-Load-Bearing Conditions—Temperature

The experimental results are shown in Figure 9. As the temperature increases, the corrosion rate of the Q125 steel sheet decreases. The corrosion rate of 3Cr steel sheets shows a trend of first increasing and then decreasing with the increase in temperature, and the corrosion rate is the highest at 90 °C. The corrosion rate of 13Cr increases with the temperature. So, Q125 has the highest corrosion rate, while 13Cr has the lowest one. The influence of temperature on CO₂ corrosion is quite complex. Within a certain temperature range, the dissolution rate of steel in a CO₂ solution increases with the increase in temperature. When a dense corrosion-product film is formed on the surface of carbon steel, the dissolution rate of the steel in a CO₂ aqueous solution decreases with increasing temperature. The temperature at which the corrosion rate of different steels reaches its peak is not consistent, which is determined by material characteristics. For Q125, which has a relatively weak corrosion resistance, the peak corrosion rate corresponds to a temperature of around 80 °C, which is consistent with the research results. 13Cr, with the highest chromium content, does not have a peak corrosion rate at the current corrosion temperature.

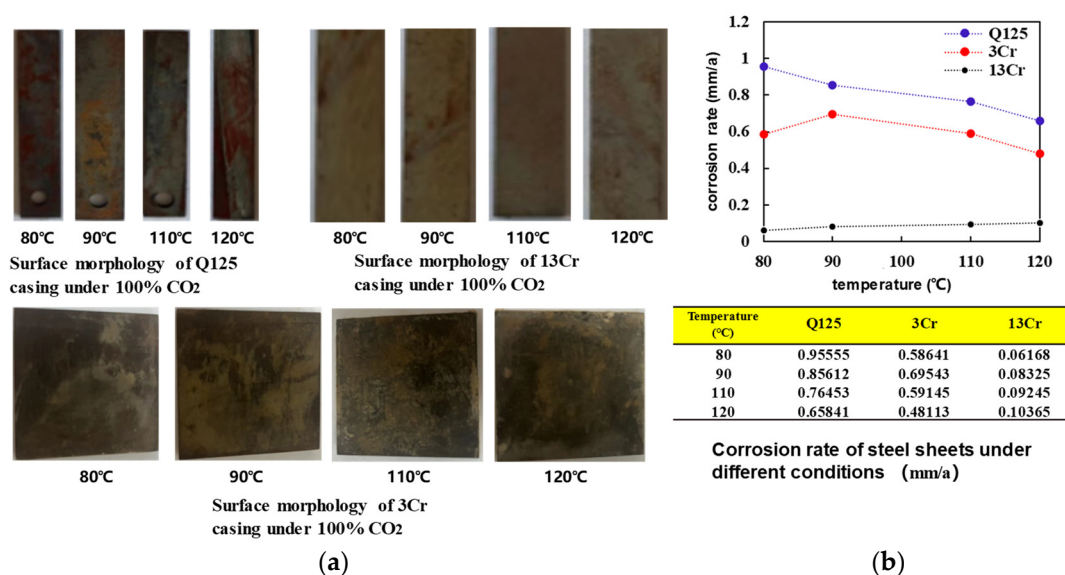


Figure 9. Experimental results of CO₂ corrosion of casing under non-load-bearing conditions. (a) Photos before and after the casing corrosion rate and (b) corrosion-rate curve.

5. A Prediction Method for Wellbore Damage under Fracturing and CO₂ Long-Term Corrosion Conditions

5.1. Wellbore Damage Failure Modes

There are three failure modes of wellbore integrity under fracturing and CO₂ long-term corrosion conditions:

- (1) Failure of the cement-sheath body—the cementing interface is well cemented, but tensile failure occurs due to insufficient strength of the cement-sheath body;
- (2) Micro-annular gap at the casing–cement sheath interface—the cementing interface is imperfect, and micro-annular gap occurs due to the discontinuity of interface displacement during loading-unloading;
- (3) Channeling fractures are formed at the cement sheath–formation interface—during the fracturing process, channeling channels are formed due to the initial damage and expansion of the fracturing fluid along the interface. According to the conditions of fracturing and long-term CO₂ corrosion, the schematic diagram describing the wellbore damage prediction is shown in Figure 10.

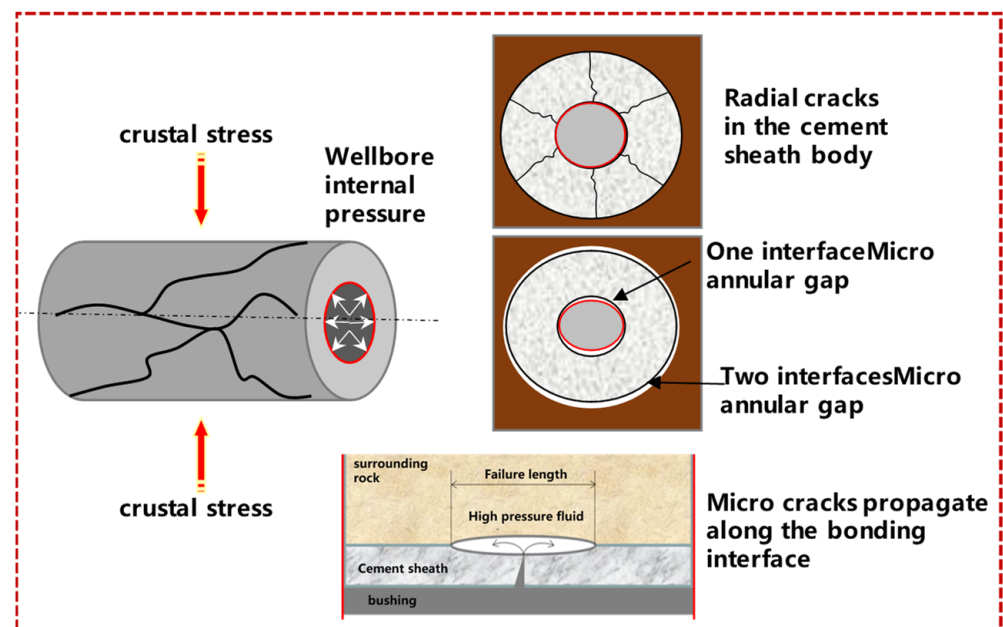


Figure 10. Schematic diagram of wellbore failure.

5.2. Stress Distribution of the Loading Process Assembly

5.2.1. Casing Stress

A stress model is established for the combination of casing, cement sheath, and formation, and the variation law of casing stress with wellbore internal pressure is analyzed. The initial parameters of the geometric model are shown in Table 1 and the material parameters and boundary conditions are shown in Table 2.

Table 1. Initial parameters of geometric model.

Inner Diameter of Casing/mm	Inner Diameter of Cement Ring/mm	Infinite Stratum	
		Inner Diameter/mm	External Diameter/mm
118.6	139.7	215.9	1000

As shown in Figure 11, in the unloading stage, under the action of non-uniform in-situ stress, the maximum effective stress of the casing appears on the inner wall of the casing

(358 MPa), and the internal pressure of the wellbore and the in situ stress act together on the wellbore assembly during loading. The compressive stress of the casing is relieved at the initial stage of the application of the internal pressure of the wellbore, the effective stress of the casing gradually increases with the increase of the internal pressure of the wellbore, and the effective stress of the casing is about 731 MPa under the fracturing condition ($P_{in} = 85 \text{ MPa}$).

Table 2. Material parameters and boundary conditions.

Name	Casing	Cement	Stratum
elastic modulus/GPa	210	6	20
Poisson's ratio	0.3	0.2	0.25
triaxial stress	σ_H 60 MPa	σ_h 50 MPa	σ_v 54.8 MPa

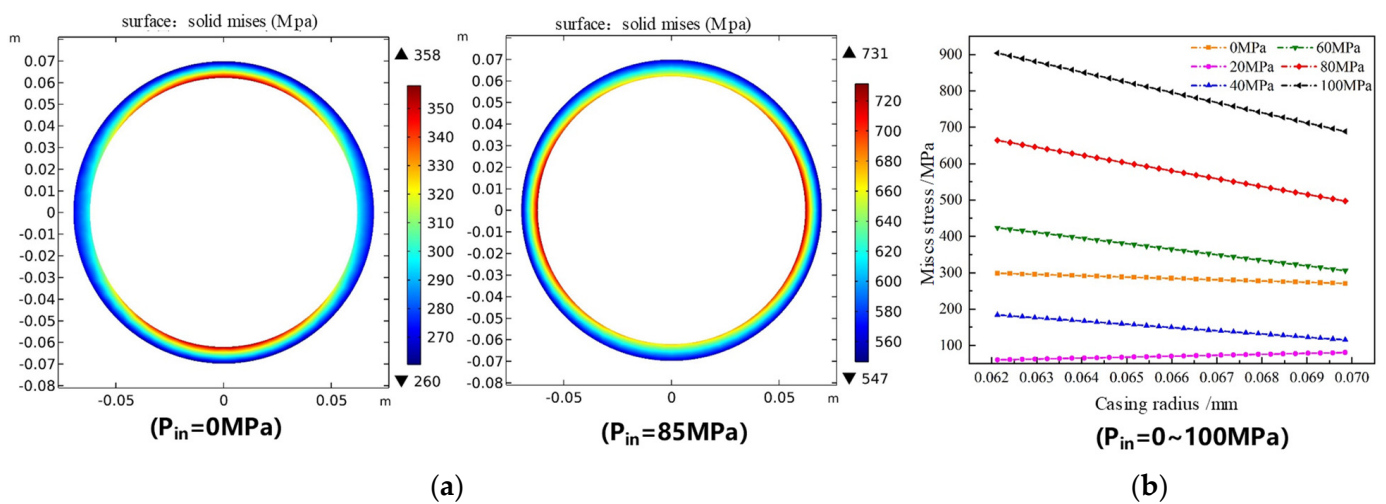


Figure 11. Contour diagram of effective stress distribution of casing and effective stress of casing during loading process. (a) Casing effective stress contour (b) Casing effective stress at 0° around the well.

5.2.2. The Mechanical Properties of the Casing and Cement Sheath Vary with the Corrosion Time and the Influence of Stress Distribution on the Assembly

As shown in Figure 12, the wall thickness of the casing decreases uniformly with the corrosion time, and the elastic modulus of the cement sheath decreases with the corrosion time, and the decrease gradually decreases. The circumferential stress of the casing increases with the extension of the corrosion time, the increase increases, and the circumferential stress does not exceed 400 MPa within 10 years of corrosion. The circumferential stress of the cement sheath decreases with the extension of corrosion time, and there is a trend of changing from compressive stress to tensile stress, but it does not exceed the tensile strength of the cement sheath and does not fail. The radial stress of the casing and the cement sheath decreases first and then increases with the corrosion time, and the compressive strength of the cement sheath does not exceed and does not fail.

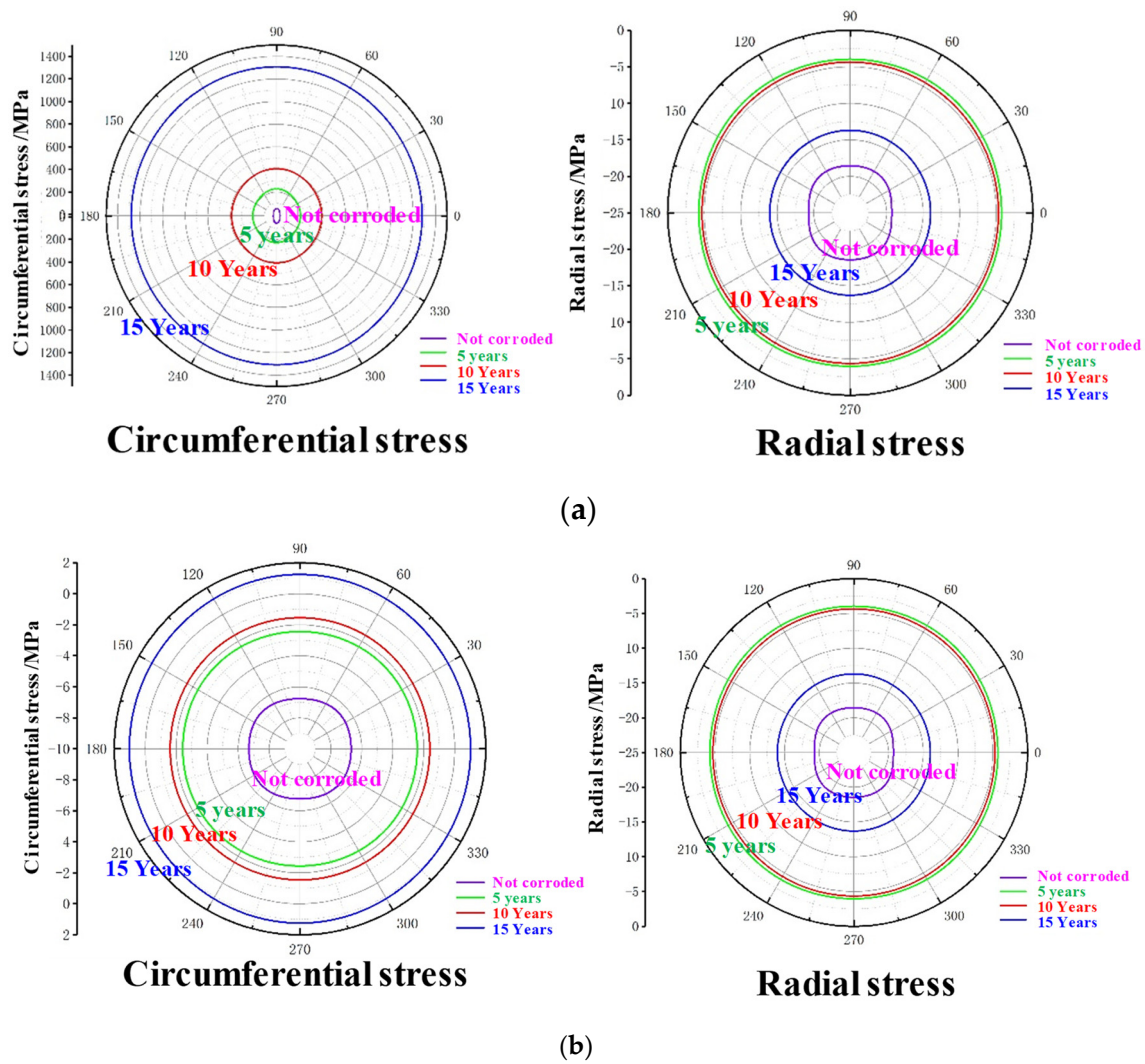


Figure 12. The stress on the outer wall of the casing and the inner wall of the cement ring. (a) The outer wall of the casing is stressed. (b) The inner wall of the cement ring is stressed.

6. Summary

- (1) The physical characteristics of CO₂ under actual formation conditions are revealed, and the change trend of CO₂ density, viscosity, and compression factor along the wellbore is calculated. The density and viscosity show a downward trend along the well depth, while the compression factor shows an upward trend;
- (2) The influence of CO₂ corrosion on the casing and cement are studied. After corrosion, the casing surface of Q125 and 3Cr has a rough and loose structure, the interface is also loose, and the morphology of 13Cr does not change significantly;
- (3) Under the corrosion condition of a CO₂ concentration of more than 50%, the corrosion depth of Q125 casing advances linearly with time, and the corrosion rate changes little with the corrosion time. The corrosion depth of the 3Cr and 13Cr casing increases slowly with the extension of corrosion time, and the corrosion rate decreases gradually;
- (4) The circumferential stress of the casing increases with the extension of the corrosion time but does not exceed 400 MPa within 10 years of corrosion. The radial stress of the casing and the cement decreases first and then increases with the corrosion time. The compressive strength of the cement sheath does not exceed the compressive strength, and no damage occurs.

Author Contributions: Conceptualization, M.C. and J.L.; methodology, M.C.; validation, W.M., N.Z. and P.W.; formal analysis, X.Z. and S.Y.; investigation, J.C.; resources, M.C.; data curation, J.L.; writing—original draft preparation, M.C.; writing—review and editing, M.C.; visualization, M.C.; supervision, J.C.; project administration, M.C.; funding acquisition, M.C. All authors have read and agreed to the published version of the manuscript.

Funding: This research was funded by the Study on Key Technologies of Production Increase and Transformation of Gulong Shale Oil (2021ZZ10-04).

Data Availability Statement: No new data were created or analyzed in this study. Data sharing is not applicable to this article.

Conflicts of Interest: Authors Meng Cai, Junliang Li, Wenhai Ma, Nan Zhang, Peng Wang and Xiaochuan Zhang were employed by the company Daqing Oil Field Production Technology Institute. Authors Shangyu Yang and Jing Cao were employed by the company CNPC Tubular Goods Research Institute.

References

- Zhang, J.; Mu, L.; Guo, Q.; Cai, Z.; Lu, F.; Jiao, Z. Research on Well Integrity during CO₂ Geological Utilization and Storage Based on CT Scanning Technique. In Proceedings of the Carbon Management Technology Conference, Houston, TX, USA, 15–18 July 2019. CMTC-553321-MS.
- Amour, F.; Hosseinzadehsadati, S.B.; Hajiabadi, M.R.; Nick, H.M. Shear and vertical deformation behaviour at the field scale during CO₂ storage in a depleted chalk reservoir (Danish North Sea). In Proceedings of the 57th US Rock Mechanics/Geomechanics Symposium, Atlanta, GA, USA, 25–28 June 2023. ARMA 23–673.
- Lüftenegger, M.; Rath, A.; Smith, M.; Danilko, A. CO₂ Injection in a Depleted Gas Field. In Proceedings of the SPE/IATMI Asia Pacific Oil & Gas Conference and Exhibition, Jakarta, Indonesia, 10–12 October 2023. SPE-212589-MS.
- Gu, C.; Su, F.; Feng, Y.; Li, X.; Deng, J. Investigation on Radial Crack of Cement Sheath During CO₂ Injection Using a TM-XFEM Coupled Model. In Proceedings of the 57th US Rock Mechanics/Geomechanics Symposium, Atlanta, GA, USA, 25–28 June 2023. ARMA 23–525.
- Zhang, W.; Liao, W.; Eckert, A.; Ma, H.; Prevallet, A.; Goedde, T.; Wronkiewicz, D.; Meng, M. Wellbore integrity evaluation for CO₂ sequestration wells: An integrated experimental, geochemical, and numerical investigation. In Proceedings of the 56th US Rock Mechanics/Geomechanics Symposium, Santa Fe, NM, USA, 26–29 June 2022. ARMA 22–816.
- Dian, W.; Jun, L.; Xianbo, L.; Tuo, L.; Penglin, L.; Wei, L. Analysis of cement plug bonding surface integrity in CO₂ geological storage. In Proceedings of the 56th US Rock Mechanics/Geomechanics Symposium, Santa Fe, NM, USA, 26–29 June 2022. ARMA 22–213.
- Meng, M.; Frash, L.P.; Chen, B.; Welch, N.J.; Li, W.; Carey, J.W. Experimental study of water and CO₂ transport along the casing-cement interface. In Proceedings of the 55th US Rock Mechanics/Geomechanics Symposium, Houston, TX, USA, 20–23 June 2021. ARMA 21–1196.
- Xie, X.; Edvardsen, L.; Cerasi, P. CO₂-induced creep on Draupne shale and impact on cemented wellbore integrity. In Proceedings of the 55th US Rock Mechanics/Geomechanics Symposium, Houston, TX, USA, 20–23 June 2021. ARMA 21–1399.
- Wise, J.; Nygaard, R.; Hareland, G. Numerical Analysis of Wellbore Integrity and Cement Sheath Debonding for Wells in the Eugene Island OPD, Gulf of Mexico. In Proceedings of the 53rd US Rock Mechanics/Geomechanics Symposium, New York, NY, USA, 23–26 June 2019. ARMA 19–439.
- Wan, T.; Zhang, J.; Dong, Y. The impact of fracture network on CO₂ storage in shale oil reservoirs. *Geoenergy Sci. Eng.* **2023**, *231*, 212322. [[CrossRef](#)]
- Sobolik, S.R.; Gomez, S.P.; Matteo, E.N.; Dewers, T.A.; Newell, P.; Stormont, J.C.; Reda Tha, M.M. Geomechanical Modeling to Predict Wellbore Stresses and Strains for the Design of Wellbore Seal Repair Materials for Use at a CO₂ Injection Site. In Proceedings of the 49th US Rock Mechanics/Geomechanics Symposium, San Francisco, CA, USA, 28 June–1 July 2015. ARMA 15–290.
- Roy, P.; Morris, J.P.; Walsh, S.D.C.; Iyer, J.; Carroll, S. Effect of thermal stress on wellbore integrity during CO₂ injection. *Int. J. Greenh. Gas Control.* **2018**, *77*, 14–26. [[CrossRef](#)]
- Kuang, N.-J.; Zhou, J.-P.; Xian, X.-F.; Zhang, C.-P.; Yang, K.; Dong, Z.-Q. Geomechanical risk and mechanism analysis of CO₂ sequestration in unconventional coal seams and shale gas reservoirs. *Rock Mech. Bull.* **2023**, *2*, 100079. [[CrossRef](#)]
- Lemaire, P.; Vasilache, M.; Dailey, C.; Ghaderi, A.; Barrabino, A.; Crandall, D.; Moore, J.; Tapiyal, D.; Beckman, E.; Enick, R. Using high pressure solutions of polyfluoroacrylate and CO₂ to Seal cement cracks for improved wellbore integrity. *Geoenergy Sci. Eng.* **2023**, *230*, 212038. [[CrossRef](#)]
- Bagheri, M.; Shariatipour, S.M.; Ganjian, E. Parametric study on the integrity of wellbores in CO₂ storage sites. *Constr. Build. Mater.* **2021**, *268*, 121060. [[CrossRef](#)]
- Liu, Y.; Liu, Q. Review of gel systems for CO₂ geological storage leakage and conformance control for enhanced oil recovery: Mechanisms, recent advances, and future perspectives. *J. Nat. Gas Sci. Eng.* **2020**, *74*, 103097. [[CrossRef](#)]

17. Dong, X.; Duan, Z.; Gao, D. Assessment on the cement integrity of CO₂ injection wells through a wellbore flow model and stress analysis. *J. Nat. Gas Sci. Eng.* **2020**, *74*, 103097. [[CrossRef](#)]
18. Song, Y.; Jun, S.; Na, Y.; Kim, K.; Jang, Y.; Wang, J. Geomechanical challenges during geological CO₂ storage: A review. *Chem. Eng. J.* **2023**, *456*, 140968. [[CrossRef](#)]
19. Iyer, J.; Lackey, G.; Edvardsen, L.; Bean, A.; Carroll, S.A.; Huerta, N.; Smith, M.M.; Torsaeter, M.; Dilmore, R.M.; Cerasi, P. A Review of Well Integrity Based on Field Experience at Carbon Utilization and Storage Sites. *Int. J. Greenh. Gas Control.* **2022**, *113*, 103533. [[CrossRef](#)]
20. Dalla Vecchia, F.; dos Santos, V.H.J.M.; Schütz, M.K.; Ponzi, G.G.D.; e Stepanha, A.S.d.G.; de Fraga Malfatti, C.; da Costa, E.M. Wellbore integrity in a saline aquifer: Experimental steel-cement interface degradation under supercritical CO₂ conditions representative of Brazil's Parana basin. *Int. J. Greenh. Gas Control.* **2020**, *98*, 103077. [[CrossRef](#)]
21. Gao, D.; Dou, H.; Dong, X. Research progress in wellbore cement sheath integrity under conditions of CO₂ injection and storage. *J. Yan'an Univ. Nat. Sci. Ed.* **2022**, *41*, 1–9.
22. Feng, Y.; Wang, Y.; Zhang, H.; Cui, C.; Huang, F.; Yuan, B. Influence of Wellbore Temperature Variation on Cement Ring Seal Integrity in CO₂-EOR Wells. *Sci. Technol. Innov.* **2022**, *31*, 5–8.
23. Lian, L.; Qin, J.; Yang, S.; Yang, Y.; Li, S.; Chen, X. An improved viscosity model for CO₂-crude system. *Pet. Explor. Dev.* **2014**, *41*, 648–653. [[CrossRef](#)]
24. Bertini, M.; Fiaschi, D.; Manfrida, G.; Niknam, P.H.; Talluri, L. Evaluation of the property methods for pure and mixture of CO₂ for power cycles analysis. *Energy Convers. Manag.* **2021**, *245*, 114568. [[CrossRef](#)]

Disclaimer/Publisher's Note: The statements, opinions and data contained in all publications are solely those of the individual author(s) and contributor(s) and not of MDPI and/or the editor(s). MDPI and/or the editor(s) disclaim responsibility for any injury to people or property resulting from any ideas, methods, instructions or products referred to in the content.